Steps in gas-surface reactions

Lent, R. van

Chapter 2

Experimental chapter

This thesis deals with results obtained using two ultrahigh vacuum machines: Lionfish and Boxfish. We provide a general description of the two machines. Chapter 6 details how reflection absorption infrared spectroscopy is performed at curved single crystal surfaces using Boxfish. Lionfish is described in much more detail in this chapter. In addition, our experiments involving reactions at curved surfaces benefit from proper molecular beam characterization. We have taken steps in measuring the flux and shape of the supersonic molecular beam at the sample using a stagnation tube. We present our findings and analysis in this chapter.

Curved single crystals

As described in chapter 1, catalytic activity in heterogeneous catalysis is often promoted by step edges. However, the exact role of step edges and terraces in catalytic processes is still debated in literature. Studies are still undertaken to unravel the fundamental processes that underlie catalytic reactions.

The general surface science approach uses macroscopically flat single crystal surfaces. A single crystal is grown and subsequently cut to expose a low Miller index surface. These low Miller index surfaces contain predominantly the (0 0 1), (1 1 0), or (1 1 1) facet. However, small miscuts will also introduce defects in the form of step edges and kinks. As a result, terraces on typical low miller index surfaces are on the order of several hundred nm wide. The influence of defects is usually studied using regularly stepped surfaces.[29, 49] Regularly stepped surfaces are produced by cutting the single crystal at an angle with respect to a low Miller index plane. In this way, specific terrace widths can be selected by choosing specific angles.[50] Studying the influence of terrace width or step density generally involves using multiple single crystals.

A variation on this approach is the use of curved single crystal surfaces. The crystal is then cut as (a section of) a cylinder[32] instead of a macroscopically flat disk. The angle with low miller index surfaces can be varied smoothly by following the curvature of the crystal, exposing a plethora of surface structures. The crystals used throughout this thesis are cut such that a low miller index surface is located at the apex of the curved surface. The 31° macroscopic curvature of the surface results in monatomic step edges and, as such, the step density varies smoothly from approximately 0.001 nm^{-1} at the apex to 1 nm^{-1} at the sides. For face centered cubic crystals, such as our platinum sample, the (1 1 1) surface separates stepped surfaces containing {0 0 1} steps on one half of the sample and {1 1 0} on the other half. The surface structure then varies from Pt(3 3 5) on one side, to Pt(1 1 1) at the apex, and Pt(5 5 3) on the other side.

The curved platinum crystal (Surface Preparation Lab) is similar to a curved Ag(1 1 1) crystal described previously.[37] The sample can be pictured as a thin circular section normal to the axis of a complete cylinder; this parent cylinder has its axis in the [1 $\bar{1}$ 0] direction and a radius of $r = 15.0$ mm. The section is 8 mm in diameter, therefore it encloses 31° of cylindrical azimuth, chosen such that the apex is a (1 1 1) plane of the FCC structure of bulk Pt. The curvature is created by spark erosion and sanding, after which the surface is polished in an automated, custom-built polishing machine (Surface Preparation Lab). The curvature of the crystal imposes a gradual increase in monatomic step density[36] as a function of azimuthal distance from the apex. The (1 1 1) terraces are separated by {0 0 1} (A-type) steps on one half of the crystal, and {1 1 0} (B-type) steps on the other half. The separation of the two step types is verified using temperature programmed desorption.[51] Thus the crystal encompasses surface structures ranging from Pt(3 3 5) at −14.4° to Pt(5 5 3) at +12.3°. The curved single crystal is mounted in a 10 mm square tantalum holder that is encased in Pt foil to prevent tantalum contamination.

Microscopic techniques, such as scanning tunneling microscopy (STM), sample a small surface area of the crystal on the order of 2 x 2 μm^2. With such high spatial resolution, it is quite straightforward to disentangle contributions by terraces and step edges. This is not possible for macroscopic techniques – terraces and steps are sampled simultaneously. This is also true for macroscopic techniques used on flat single crystal surfaces due to inevitable miscuts.

All techniques used throughout this thesis are macroscopic and convolute over a range of surface structures along the curved surface. The electron beam used in LEED probes a diameter (ϕ) or area (step density) of $\sim$ $\phi = 1$ mm (± 0.15 nm^{-1}, chapter 6) or $\sim$ $\phi = 0.35$ mm (± 0.05 nm^{-1}, chapters 3 and 4). The focused IR beam used for RAIRS in chapter 6 creates an approximately 6 mm long oval at the surface with FWHM $\sim$ 0.72 mm (± 0.11 nm^{-1}). The supersonic beam is skimmed to a rectangle of 0.5 x 6.4 mm^2 (± 0.07 nm^{-1}, chapter 4) or 0.135 x 6 mm^2 (± 0.02 nm^{-1},

chapters 3 and 4). Limiting the footprint of experimental techniques also limits the convolution over different surface structures. However, it generally reduces the signal-to-noise ratio as well. Signal averaging becomes crucial in the molecular beam experiments. The signal averaging method used throughout this thesis for King and Wells experiments is described in more detail in chapter 2.

Boxfish

Boxfish is the ultrahigh vacuum (UHV) apparatus used in chapter 6. It is a UHV chamber with a base pressure of 2×10^{-10} mbar. It is equipped with a LEED/Auger system (VG, RVL - 900), a quadrupole mass spectrometer (Pfeiffer, QMA 200), a sputter gun (IS40C1, PreVac), and an external Fourier transform infrared spectrometer (Bruker, Vertex 70) for RAIRS.

The crystal holder is suspended from a bath-type liquid nitrogen cryostat on a x, y, z, ϕ manipulator. The liquid nitrogen level is kept at approximately 50% to avoid contraction or expansion of the cold finger and consequential motion of the sample. The sample holder is electrically isolated from the cryostat and the rest of the machine by AlN plates. The crystal is heated by radiative heating and electron bombardment using a commercial filament (Osram, 150 W). High temperatures (> 600 K) are achieved by applying a positive bias to the crystal. The curved Pt surface is cleaned through multiple cycles of Ar^+ sputtering (Messer, 5.0; 400 K; 0.5 μA; 45°; 10 min; 0.25 kV), followed by O_2 treatment (Messer, 5.0; $3.5 \cdot 10^{-8}$ mbar; 900 K; 3 min) and *in vacuo* annealing (1200 K; 3 min). Three cleaning cycles were performed every day prior to experiments. The surface structure was verified using LEED. (Chapter 6) The sample was annealed for 3 min at 1200 K between individual measurements to ensure the quality of the surface.

Lionfish

Lionfish is the UHV apparatus used in chapters 3, 4, and 5. It has a base pressure of $< 1.0 \cdot 10^{-10}$ mbar. The main feature of this apparatus are the two molecular beams; a double differentially pumped supersonic molecular beam (SSB), and a single differentially pumped effusive beam (EB). The molecular beams cross at 45° at the sample. Additionally, the apparatus contains: a four-grid MCP LEED/Auger (BLD800IR, OCI Vacuum Microengineering), a quadrupole mass spectrometer (QMA 200, Pfeiffer vacuum), and a quadrupole mass spectrometer (UTI-100C) that can be translated along the SSB axis for time of flight spectroscopy (TOF).

Single crystal samples are mounted on a x, y, z, ϕ manipulator. The sample temperature is measured using a K-type thermocouple. The crystal is cooled using a bath liquid nitrogen cryostat and heated via radiative heating and electron bombardment by a tungsten filament (Osram). A bias potential can be applied to the sample or the filament to increase the electron bombardment efficiency so that the required temperatures can be reached. The curved Pt surfaces are cleaned by Ar sputtering ($6{\cdot}10^{-6}$ mbar, Messer 5.0, 45°, 900 K, 0.5 kV, 1 μA), O_2 annealing (900 K, $3{\cdot}10^{-8}$ mbar, Messer 5.0) and 1200 K *in vacuo* annealing. For the final cleaning cycle, O_2 annealing and 1200 K annealing are replaced by 900 K *in vacuo* annealing to avoid O_2 induced step doubling or high temperature induced faceting.

Supersonic molecular beam

Supersonic molecular beams are a powerful tool for studying gas-surface dynamics. The supersonic expansion results in cooling of molecules in the molecular beam, thereby narrowing translational and rotational distributions. Vibrational cooling is inefficient. In contrast to translational and rotational energy, vibrational energy is generally too large to be dissipated through collisions. The kinetic energy of the molecular beam can be varied by seeding into lighter gases, anti-seeding into heavier gases, or by vary-

ing the expansion temperature. Additionally, the internal energy increases only with expansion temperature or optical excitation (chapter 7).

A cut-through of the supersonic molecular beam (SSB) is shown in figure 2.1. The supersonic molecular beam consists of three differentially pumped stages – the source chamber (SSB1, green), first differentially pumped stage (SSB2, blue), and the second differentially pumped stage (SSB3, red) – attached to the main chamber (orange). The molecular beam is formed in the source chamber by expanding a constant flow of gas from a tungsten nozzle with a 28 µm laser drilled orifice. The nozzle temperature is measured using a C-type thermocouple laser welded to the nozzle. The temperature of the nozzle can be controlled by radiative heating; a ring surrounding the nozzle can be heated through electron bombardment by two filaments (Osram). Heat shields protect the rest of the system from warming up. A skimmer (diameter $\phi = 0.45$ mm) separating SSB1 and SSB2 selects the coldest part of the expansion.

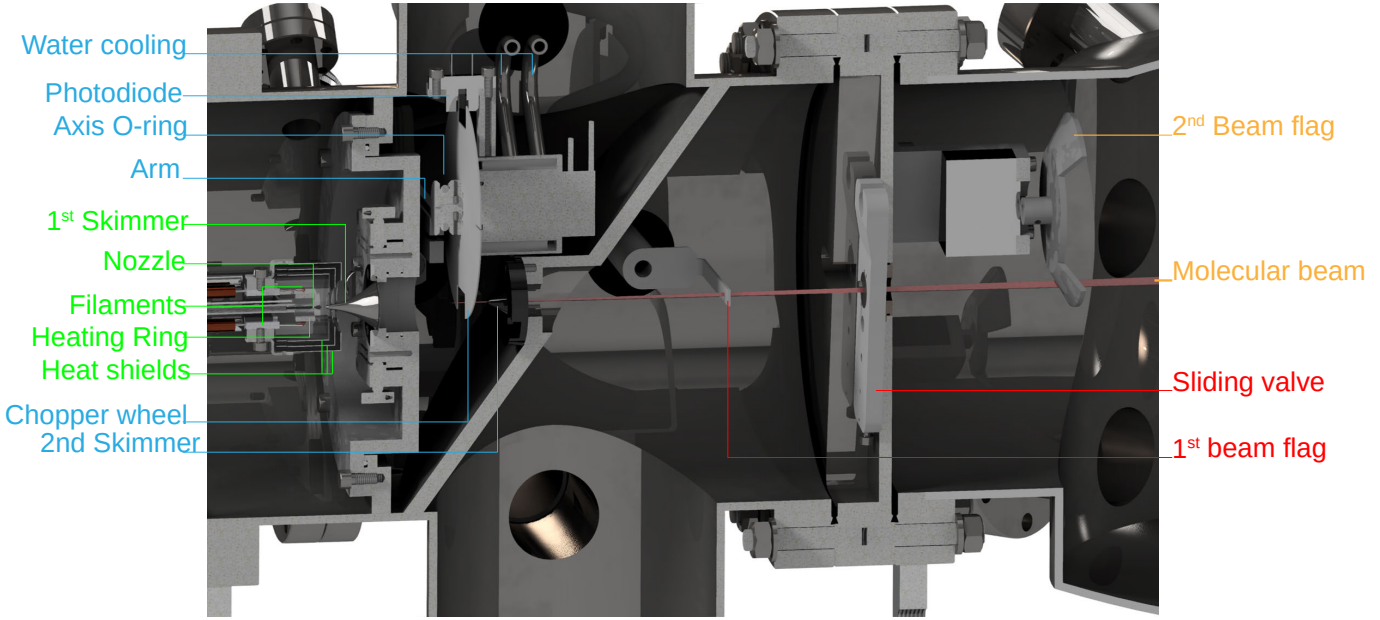

Figure 2.1: A cut-through of the supersonic molecular beam showing its various parts in the source chamber (SSB1, green), first differentially pumped stage (SSB2, blue), second differentially pumped stage (SSB3, red), and main chamber (orange).

SSB2 contains a water-cooled brushless motor (2444 S 024 B, Faulhaber). It chops the molecular beam for TOF or reduces the number of molecules striking the surface by its duty cycle(16%). The chopper wheel contains two 0.85 mm and two 17 mm slots chopping the beam at a radius of approximately 56.0 mm. The chopper frequency is measured with an optical sensor (TCSS 2100). The chopper can be opened by translating a stainless steel arm onto the axis O-ring while monitoring the pressure in the second differentially pumped stage. A second skimmer (ϕ = 2.5 mm) separates the SSB2 from SSB3.

The second differentially pumped section contains a stainless steel beam flag used for King and Wells experiments. The flag is operated through a Labview controlled solenoid valve. The molecular beam is shaped by one of four different orifices: ϕ = 1.8 mm (chapter 5), 3.2 mm, 6.2 mm, and a slit). Throughout this thesis, two different slit sizes are used: 0.25 x 3 mm^2 (chapter 4) and 0.065 x 3 mm^2 (chapters 3 and 4). The orifice is selected with the sliding valve separating SSB3 from the main chamber.

As the molecular beam enters the main chamber, it can be interrupted prior to impinging upon the crystal using a second beam flag. This beam flag is driven by a UHV compatible stepper motor (C14.1, Arun Microelectronics Ltd). The beam flag is operated manually (chapter 5) or by sending commands to the stepper motor controller (SMD210, Arun Microelectronics Ltd) with labview (chapters 3 and 4). With the flag opened, the molecular beam is free to impact the surface or, when the crystal is translated out of the molecular beam path, fly into the on-axis mass spectrometer for time of flight spectroscopy.

Forming a supersonic molecular beam

Three flow controllers (Bronkhorst) feed the supersonic beam with gases. The thermal mass flow controllers (MFC) use the thermal conductivity of gases to measure and then regulate the flow using a control valve. These

flow controllers are calibrated for N_2 flow but can be corrected for different gases using the Bronkhorst developed FLUIDAT® website.

A gas mixture is created using the flow controllers. The supersonic beam is formed by expanding this gas mixture from the tungsten nozzle into the source chamber. The pressure inside the nozzle – measured with a capacitance manometer (MKS, 750C14MC02GA) – stabilizes after some time. Figure 2.2 shows that the equilibrated nozzle pressure is proportional with flow, but that the expansion is gas specific (the pressure drop over a tube has a viscosity dependence).

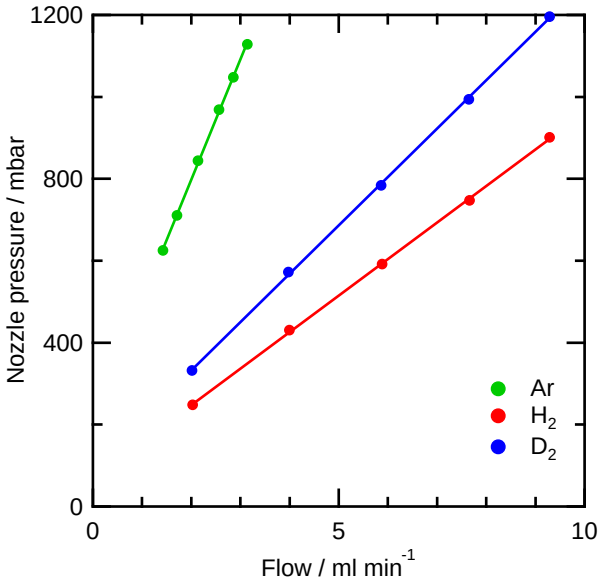

Figure 2.2: Nozzle pressure dependence on flow for pure Ar, D_2, and H_2 expansions.

The flows shown in figure 2.2 are significantly smaller than the available range of the flow controllers (10, 20, and 50 ml min^{-1}). The flow (or nozzle pressure) available is limited by the pressure in the source chamber and its fore-vacuum pump. The flow out of the nozzle orifice depends on the nozzle pressure, gas type, and orifice diameter. Since the pressure inside the nozzle

takes time to stabilize, the flow into the source chamber also takes time to stabilize. As a result, it takes some time for the source chamber pressure to equilibrate. SSB1, SSB2, and SSB3 are each pumped by a turbo molecular pump (TMU 521P, Pfeiffer Vacuum; HiPace 300, Pfeiffer Vacuum; TMU 261P, Pfeiffer Vacuum), each backed by a rotary vane pump (DUO 30A, Pfeiffer Vacuum; 2010, Alcatel; E2M5, Edwards). The pressures in SSB1 and SSB3 are measured using a cold cathode pressure gauge (IKR 270, Pfeiffer Vacuum), while the pressure in SSB2 is measured using a full range pressure gauge (PKR 251).

The pressures inside the source and differentially pumped chambers are shown in figure 2.3. The equilibrium pressure in the source chamber is dominated by the flow from the nozzle, the average molecular mass of the gas inside the nozzle, and the pumping speed of the turbo molecular pump. The observed non-linear behavior is likely due to the increased fore-vacuum pressure, which were not actively monitored during these experiments. In contrast, the pressure in both SSB2 and SSB3 is approximately linear with the flows and nozzle pressures used here. The gas load on the pumps is much smaller and pressure build up at the back of the turbo molecular pump is not an issue for SSB2 and SSB3.

Flux measurement

The pressures in the supersonic molecular beam are important parameters for starting experiments. More important for experimental conditions are the flux and footprint of the molecular beam at the surface. Both are measured by exchanging the sample manipulator with a stagnation tube. The stagnation tube is schematically shown in figure 2.4. A $\phi = 6$ mm tube is suspended from a x, y, z manipulator. At the crystal position, a 1 mm hole is drilled into the tube, after which the area around the orifice is milled to a wall thickness of ~ 0.3 mm. The tube has a 45° plate behind orifice so that molecules flying through the orifice scatter into the tube. A calibrated pressure gauge (Series 370 stabil-ion, Granville-Phillips) is mounted to the tube on an elbow at the top of the manipulator. The

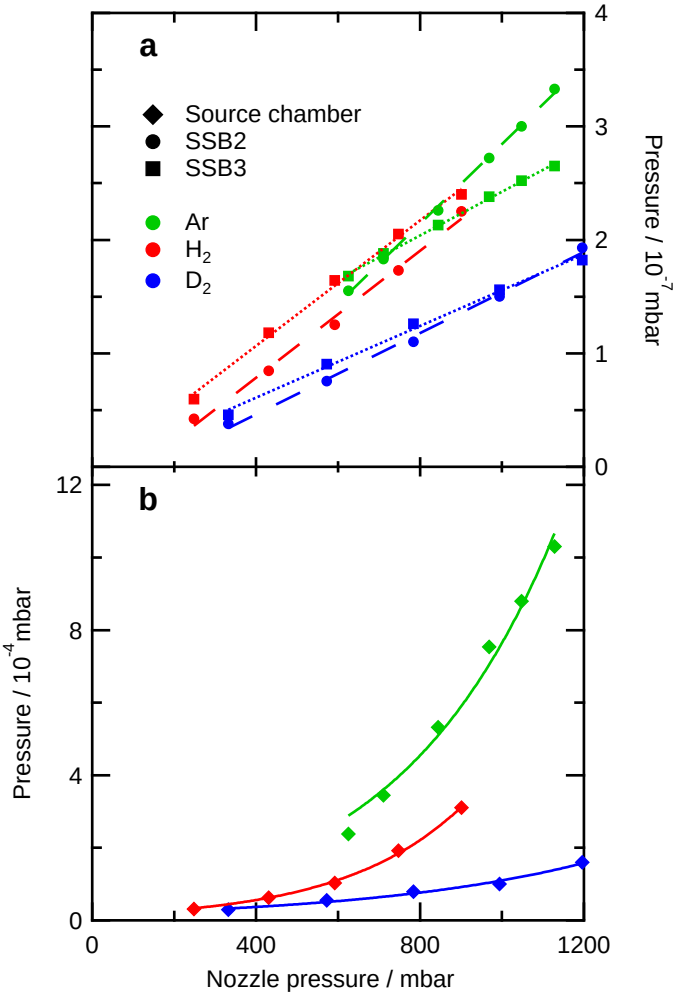

Figure 2.3: The pressure dependence of the source and differentially pumped stages on the nozzle pressure for Ar, D_2, and H_2 flows shown in Figure 2.2.

elbow reduces both the error in the volume and the stagnation tube base pressure.

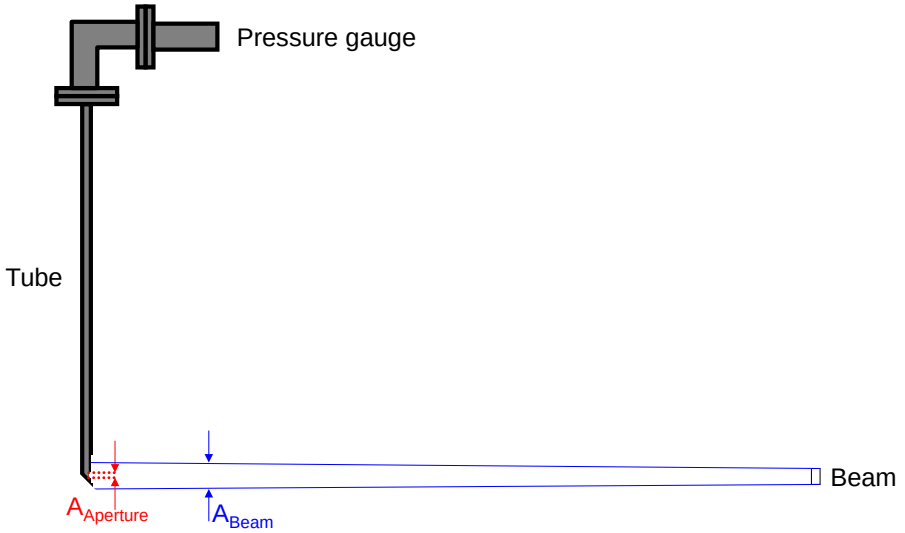

Figure 2.4: Schematic view of the stagnation tube used to measure the flux and shape of the beam.

We start with measuring the flux of the molecular beam, before determining its footprint. Prior to the beam being incident on the orifice, an equilibrium is set such that:

$$\frac{dn}{dt} = 0 \tag{2.1}$$

where n is the number of molecules. The initial pressure is governed by constant contributions: outgassing of the stagnation tube walls, residual gas molecules from the main chamber flying effusively into the stagnation tube, and molecules flying effusively out of the stagnation tube. Molecules flying effusively through an orifice is described by the collision rate with the area of the orifice. As such, when the molecular beam overlaps with the orifice, the equilibrium is disturbed by an instantaneous increase of Φ_{in} with the flux of the molecular beam, Φ_{beam}:

$$\frac{dn}{dt} = (\Phi_{in} - \Phi_{out})\ A = (\Phi_{beam} - Z_W)\, A \tag{2.2}$$

where Z_W is the collision rate in $molecules\ m^{-2}\ s^{-1}$. The change in the number of molecules can be rewritten to a change in pressure and expressed as function of the collision rate:

$$\frac{dP}{dt} = \left(\Phi_{beam} - \frac{P}{\sqrt{2\pi \frac{M}{N_A} k_B T}} \right) A \frac{k_B T}{V} \tag{2.3}$$

We now rewrite the right hand brackets in order to change the expression into a standard integral:

$$\frac{dP}{dt} = \left(1 - \frac{P}{\Phi_{beam} \sqrt{2\pi \frac{M}{N_A} k_B T}} \right) \Phi_{beam} A \frac{k_B T}{V} \tag{2.4}$$

The integral can then be set up:

$$\int_0^P \frac{1}{1 - \frac{P}{\Phi_{beam} \sqrt{2\pi \frac{M}{N_A} k_B T}}} dP = \int_0^t \Phi_{beam} A \frac{k_B T}{V} dt \tag{2.5}$$

and is solved using the standard integral:

$$\int \frac{1}{b + ax} = \frac{1}{a} ln|ax + b| \tag{2.6}$$

It results in the following expression:

$$-\Phi_{beam} \sqrt{2\pi \frac{M}{N_A} k_B T}\, ln|1 - \frac{P}{\Phi_{beam} \sqrt{2\pi \frac{M}{N_A} k_B T}}| = \Phi_{beam} A \frac{k_B T}{V} t \tag{2.7}$$

Isolating P results in:

$$P = \Phi_{beam} \sqrt{2\pi \frac{M}{N_A} k_B T} \left((1 - e^{\left(- \frac{A \frac{k_B T}{V}}{\sqrt{2\pi \frac{M}{N_A} k_B T}} t \right)} \right) \tag{2.8}$$

In the limit of large t, the pressure in the stagnation tube is then a function of Φ_{beam} in the following way:

$$P = \Phi_{beam} \sqrt{2\pi \frac{M}{N_A} k_B T} \tag{2.9}$$

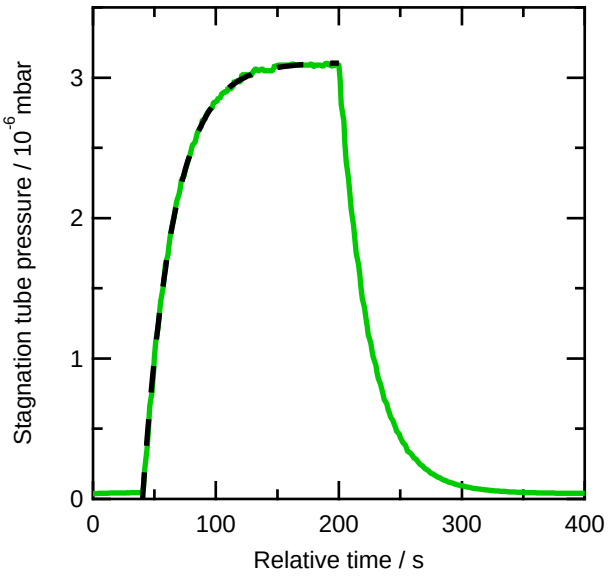

Figure 2.5: The pressure inside the stagnation tube as a function of time. The beam is opened to the main chamber at t = 0. At t = 40 s, the flag inside the main chamber is opened so that the beam directly impinges unto the orifice into the stagnation tube. After impinging for 160 s, the beam is switched off causing the pressure to drop. The black dashed line is a exponential fit to the data.

Figure 2.5 shows an example of the recorded data for an Ar beam. The pressure measured with the calibrated pressure gauge is recorded from the analog controller output using Labview. The data is fitted with a general fit function based on equation 2.8 (dashed black line) to extract the stagnation pressure. The beam flux is calculated from the stagnation pressure using equation 2.9.

The calculated flux for different flows of Ar, H_2, and D_2 beams are presented in figure 2.6. The flux for the three different gases show a linear dependence over the range measured. Unfortunately, the flux for mixed beams cannot be determined through extrapolation of the pure beams. These may be determined by repeating the experiments outlined here, but starting from a mixed beam and varying the flow of one of the constituents

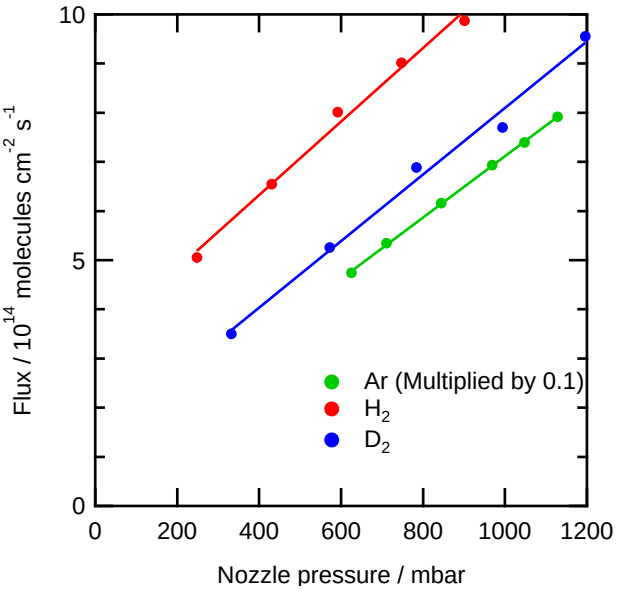

Figure 2.6: Flux dependence on nozzle pressure for Ar, D_2, and H_2 beams shown in figure 2.2. Note that the flux from the Ar beam is multiplied by 0.1.

at a time. These results present a reasonable estimate for beam fluxes used throughout this thesis.

Beam profile

Throughout this thesis, the molecular beam is combined with curved single crystal surfaces to study the effect of step density on dissociation and catalytic activity. The footprint of the molecular beam is a key experimental parameter due to surface structure convolutions, as detailed in chapter 2. The orifice between SSB3 and the main chamber controls the size and shape of the molecular beam.

This orifice can be varied using a sliding valve. The sliding valve contains a slit of 3 x 0.065 mm^2 (or 0.25 x 3 mm^2) and three circular orifices; ϕ = 1.8 mm, 3.2 mm, and 6.2 mm. The size of the molecular beam at the surface can be estimated from the size and distance between the sliding

valve and first skimmer orifices, and extrapolating to the surface position. We assume that the first skimmer is the point source for the molecular beam. The skimmer-orifice and skimmer-sample distances are 202.5 mm and 398.3 mm, respectively. Using simple trigonometry, we calculate a beam diameter of 3.54 mm for the smallest orifice (ϕ = 1.8 mm).

Alternatively, the footprint of the beam can be measured with the stagnation tube setup shown in Figure 2.4. Similarly to the flux measurements, the orifice of the stagnation tube is placed at the crystal position. After aligning the orifice to the center of the beam, the 1 mm orifice is traced across the molecular beam normal to the propagation axis. The beam footprint has been measured for the two beam shapes mainly used throughout this thesis: the 3 x 0.065 mm^2 slit and the 1.8 mm orifice. The experiments are performed similar to those shown in figure 2.5. An exponential fit is used to extract the stagnation pressure. The results are normalized to the maximum pressure, where the molecular beam completely covers the stagnation tube orifice.

The results for the circular orifice are shown in figure 2.7. As the orifice is translated into the beam, the pressure rises quickly until a plateau is reached where the orifice is smaller than the molecular beam. The beam pressure shows a stable value over the range where the orifice is completely overlapped by the beam. The overlap can be calculated using the standard math problem of calculating the overlap between two circles.[52] The general solution for the overlap is shown in equation 2.10.

$$A_{st\ sector} = r_{st} \cdot acos\left(\frac{d^2 + r_{st}^2 - r_b^2}{2 \cdot d \cdot r_{st}}\right)$$

$$A_{b\ sector} = r_b \cdot acos\left(\frac{d^2 + r_b^2 - r_{st}^2}{2 \cdot d \cdot r_{st}}\right)$$

$$A_{correction} = \frac{1}{2}\sqrt{(-d + r_{st} + r_b)(d + r_{st} - r_b)(d - r_{st} + r_b)(d + r_{st} + r_b)}$$

$$A_{overlap} = A_{st\ sector} + A_{b\ sector} - A_{correction} \tag{2.10}$$

where r_{st} and r_b are respectively the radius of the stagnation tube orifice and the radius of the molecular beam, while d is the distance between the

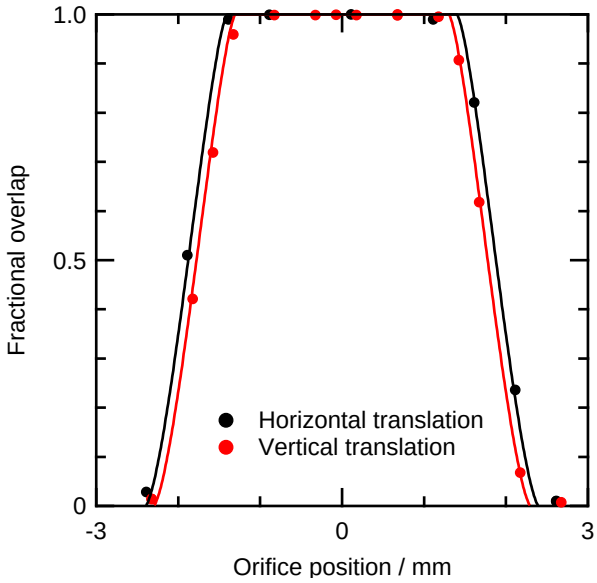

Figure 2.7: Beam profile experiment of a molecular beam shaped with the 1.8 mm diameter orifice. The beam profile is shown as the fractional overlap of the stagnation tube orifice with the molecular beam as a function of on-axis horizontal and vertical displacement. Solid lines are simulated data using the Igor procedure in appendix A. There, a beam radius of 1.9 mm and 1.8 mm are used for respectively horizontal and vertical translation impinging onto a 0.5 mm radius orifice.

center of the two circles. Using the Igor procedure in Appendix A, the overlap is calculated numerically. A few logic operators are included in the procedure to account for either circle being smaller than the other. The results are shown in figure 2.7. The calculated overlap agrees well with the measured data, but suggest that the molecular beam may be slightly elliptical. A slight misalignment could have caused the orifice to be translated off-center with respect to the molecular beam producing the same result. The results suggest that the molecular beam has a 3.8 mm diameter as it impinges onto the surface.

A similar analysis is applied to a beam shaped by a slit aperture translates over the stagnation tube orifice. The overlap is calculated by summing

the area of all different sections when the rectangular beam overlaps the circular orifice. The procedure used to calculate the overlap for vertical and horizontal translation can be found in Appendix A.

Experimental results are shown with simulated beam profiles in figure 2.8. Spread in the horizontal translation data is caused by hysteresis in the x-y manipulator. The calculated overlap shows that the footprint of the molecular beam at the sample is 6.0 x 0.126 mm^2.

The beam size we report here are somewhat larger than suggested by the calculated 3.54 mm. They are even larger than 3.0 mm reported by Cao.[53] However, the previous results are too narrow for the reported data; the simulated line falls well between the data and easily explains part of the discrepancy ($\sim$0.5 mm). While presumably not essential to their simulated results, the reported orifice sizes are also incorrect. A smaller discrepancy may also stem from the stagnation tube orifice either not being symmetric or having a diameter somewhat smaller than 1 mm. We have not verified the orifice shape after identifying the discrepancy with the previous data and calculated results.

Experimental techniques

A number of experimental techniques are applied throughout this thesis. We now provide a basic description for the most important techniques, starting with a description of LEED and RAIRS as used on Boxfish for chapter 6. Thereafter, we provide a description of time of flight, our analysis thereof, and finish with a description of the King and Wells technique used for measuring sticking probabilities.

Low energy electron diffraction

Low energy electron diffraction (LEED) is used throughout this thesis to verify the structure of the single crystal surfaces. A generic 3-grid LEED is shown in figure 2.9. In LEED, an electron gun sends a beam of electrons at the surface. The sample is placed in both the focus of the electron beam

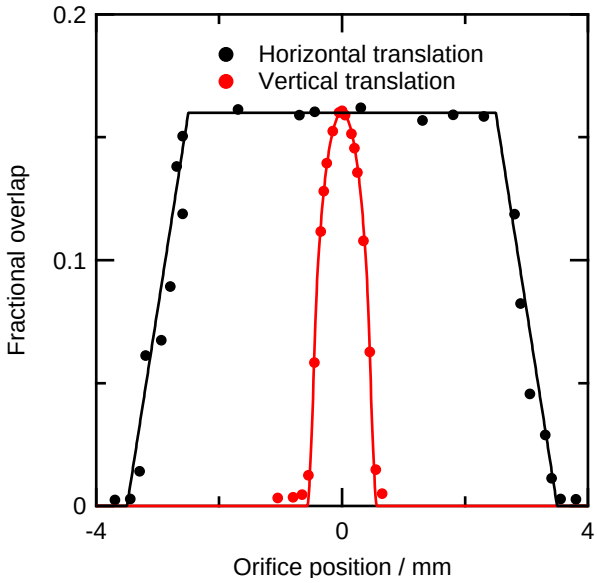

Figure 2.8: Beam profile results for a molecular beam shaped with a 0.065 x 3 mm slit orifice. The beam profile is the fractional overlap of the stagnation tube orifice with the molecular beam as a function of horizontal and vertical displacement. Solid lines are simulated with Igor procedures in appendix A and A. There, the molecular beam is a 6.0 x 0.126 mm rectangle impinging onto a 0.5 mm radius orifice.

and the origin of the three (or four) concentric spherical grids. Electrons may scatter elastically or inelastically from the surface. The grids filter out inelastically scattered electrons, while elastically scattered electrons pass through to hit a phosphorescent screen. They show up as green dots, which form a diffraction pattern. From the resulting pattern the average surface structure can be derived. Regularly stepped surfaces cause an additional splitting in the diffraction pattern by introducing an additional diffraction grating, such as shown in figure 1.3b.

Reflection absorption infrared spectroscopy

Reflection Absorption Infrared Spectroscopy (RAIRS) is the characteristic technique used on Boxfish. Surface vibrational spectroscopic methods are powerful techniques for identifying adsorbates, but RAIRS can also be

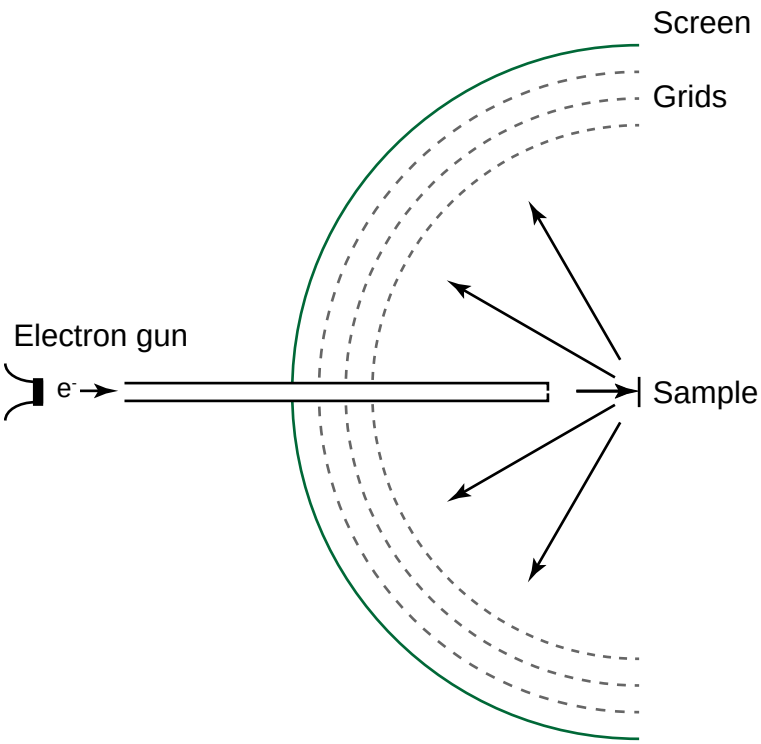

Figure 2.9: Schematic overview of a generic 3-grid low energy electronic optic.

used to extract details, e.g. on interactions between adsorbates or surface binding sites.

RAIRS is a spectroscopic technique which works in the infrared region. To describe how RAIRS works, it is convenient to describe infrared radiation as a wave with an electric and magnetic field vector. Molecules can absorb infrared radiation if the electric field of the infrared radiation resonates with the electric field of the transition dipole. Infrared absorption increases with the overlap between the electric field of the infrared radiation and the transition dipole moment. Absorption of infrared radiation by molecules leads to excitation of molecular vibrations. In order to excite a vibration in the molecule, there has to be a change in the dipole moment. This is the selection rule for infrared absorption.

When a dipole is adsorbed to a conducting surface, the surface creates a mirror image of the dipole through its electrons. Depending on the orientation of the dipole, this either cancels or doubles the effective dipole moment. The dipole moment of molecules adsorbed perpendicular to the surface is doubled, while the dipole moment is canceled when adsorbed parallel to the surface. Combined with the selection rule, this means the dipole of molecules adsorbed parallel to the surface do not absorb infrared radiation.

Only molecules with a dipole perpendicular to the surface absorb infrared radiation. The electric field vector of infrared radiation needs to have as much overlap with the dipole moment as possible, which is achieved by using polarized radiation. The polarization angle is taken with respect to the surface normal where p stands for parallel and s stands for senkrecht (German for perpendicular). As dipoles are aligned perpendicular to the surface, all interaction with infrared radiation results from p-polarized light. RAIRS is performed in reflection. It is intuitive that the amount of p-polarized radiation is a function of the angle with the surface. If the angle with the surface is 90°, there will be no p-polarized radiation possible. If the angle with the surface is a grazing angle, then a large amount of radiation can be p-polarized and there is more absorption.

Infrared (IR) experiments are generally performed using a Fourier transform infrared (FTIR) spectrometer. Boxfish uses a Bruker Vertex 70 FTIR spectrometer. Inside the FTIR spectrometer a globar radiates IR radiation. This is combined with a Helium-Neon laser used as a reference. A tungsten filament is present as a white light source within the FTIR. It provides a visual indication of the IR beam for aligning purposes. A Michelson interferometer is used to create an interference pattern in the IR radiation beam, which is required for measuring the interferogram in FTIR. Using additional mirrors, the IR radiation is reflected out of the spectrometer, which is where our setup is different from a normal FTIR spectrometer.

After exiting the spectrometer, the beam of IR radiation is steered using two gold coated mirrors to the right height and angle of incidence for the off-axis parabolic mirrors. The gold coated parabolic mirror focuses the IR beam on the sample. Prior to reflection by the sample, the radiation is polarized by a thallium bromoiodide (KRS-5) wire grid polarizer and passes through a calcium fluoride UHV compatible window. The IR beam reflects off the sample, passes out of the UHV chamber through another calcium fluoride window and is collimated again by a second gold coated parabolic mirror that is identical to the previous mirror. Finally, a third gold coated parabolic mirror focuses the IR radiation onto a liquid nitrogen cooled mercury cadmium telluride (MCT) detector, which measures the interferogram. The IR spectrum is finally calculated by applying the Fourier transform and dividing the sample measurement with a reference measurement.

Time of flight

Supersonic molecular beam techniques are a valuable tool in studying molecule-surface dynamics. As mentioned previously, supersonic molecular beam techniques give control over the kinetic energy through seeding and anti-seeding, or changing the expansion temperature. Although the kinetic energy distribution narrows from the expansion, it is critical to measure the kinetic energy distribution to account for remaining energy convolution effects in experiments. The velocity of molecules can be measured using Time of Flight spectroscopy (TOF). In TOF, the flight time of molecules traveling a known distance is measured.

As described before, Lionfish uses a continuous molecular beam. However, TOF requires it to be pulsed. The molecular beam is modulated with a mechanical chopper using two narrow and two broad slits. After some flight time, molecules cross the distance between the chopper wheel and the ionization region of the QMS. There, molecules are ionized, accelerated into the quadrupole, mass selected, and detected by a channeltron. The channeltron signal is amplified and pulses are counted using a multi-scalar

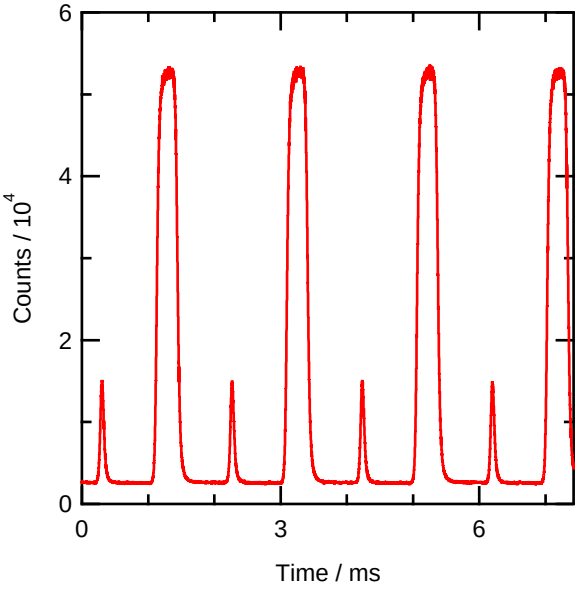

Figure 2.10: TOF spectrum of a pure D_2 supersonic beam.

card. The mass spectrometer measures for $1\frac{7}{8}$ chopper periods. The optical sensor triggers the next pulse by detecting a slit. A number of these pulses are recorded and summed up, resulting in the typical TOF spectrum shown in figure 2.10.

The most basic way of analyzing TOF is by determining the flight time for various mass spectrometer positions. The most-probable flight time can be extracted by fitting the first small peak in the TOF spectra with a Gaussian function. The velocity, $\frac{dy}{dt}$, can be directly extracted from the distance dependent most-probable flight time.

Alternatively, if the distance from the chopper to the mass spectrometer is known, the time of flight spectra can be fitted. Fitting TOF spectra has the benefit that the velocity distribution can be extracted after deconvolving any broadening effects. The TOF signals are broadened by both the pulse length of the chopper and by the length of the ionization field of the TOF mass spectrometer.

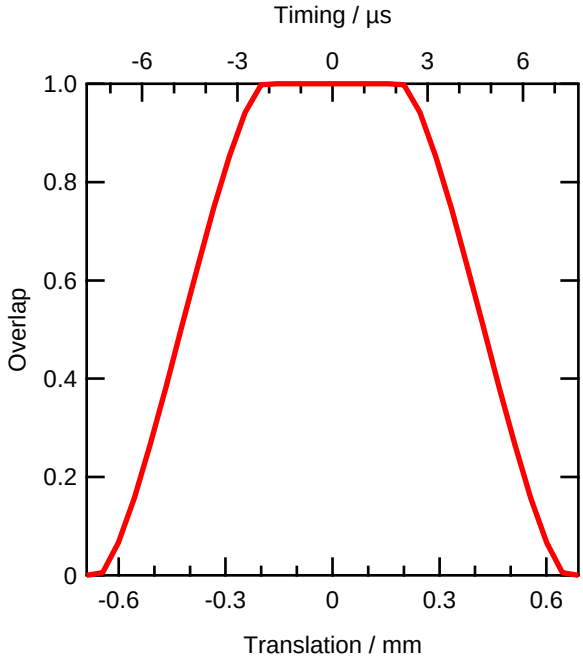

Figure 2.11: The gating function of the chopper results in a convolution.

Chopper convolution can be accounted for by broadening the fit function of the TOF spectra with the chopper gating function. We approximate the chopper slit rotating through the molecular beam by calculating the overlap of a rectangle passing over a circle, similar to the slit aperture beam profile experiments in chapter 2. Using the IGOR procedure in appendix A, the chopper gating function is calculated with the same time constant (0.5 µs) as the recorded data. The resulting gating function is shown in figure 2.11. The fit function is generated with the IGOR procedure and includes the gating function weighted time broadening.

The TOF QMS has a 3 cm long ionization region, which is beneficial for the signal-to-noise ratio of the QMS. However, it causes extra broadening. As molecules fly into the 3 cm long ionization region of the mass spectrometer, ionization may occur anywhere along its length. As a result, the neutral flight path may vary with ± 1.5 cm. We are aware of this potential

broadening mechanism but disregard its influence in our analysis.

The functional form for a TOF spectrum measured using a density sensitive detector is:[54–56]

$$f(t) = \left(\frac{l}{t}\right)^4 \cdot e^{-\left(\frac{\frac{l}{t}-\frac{l}{t_0}}{\sqrt{\frac{2RT}{M}}}\right)^2} \tag{2.11}$$

with neutral flight path l, neutral flight time t, gas constant R, gas temperature T, and molecular mass M. The neutral flight time is measured by fitting multiple TOF spectra at different positions with Gaussian functions and extrapolating to l = 0. The fit function is weighted by convoluting the neutral flight time with the pulse width due to the chopper gating function.

After fitting, the TOF spectra can be deconvoluted for the chopper gating function by using the fit function. The time of flights are converted to the flux weighted distribution by dividing the fits by velocity v.[54] The fits are then redimensioned from neutral flight time to velocity and energy using the following transformations:

Velocity:

$$v = \frac{l}{t} \tag{2.12}$$

Signal as a function of velocity:

$$\begin{aligned} \int f(t) \cdot dt &= \int f(v)\, dv \\ f(v) = f(t) \cdot \frac{dt}{dv} &= f(t) \cdot \frac{t^2}{l} \end{aligned} \tag{2.13}$$

Energy:

$$E = \frac{1}{2} m v^2 \tag{2.14}$$

Signal as a function of energy:

$$\begin{aligned} \int f(v)\, dv &= \int f(E)\, dE \\ f(E) = f(v) \frac{dv}{dE} &= f(v) \frac{t}{l} \end{aligned} \tag{2.15}$$

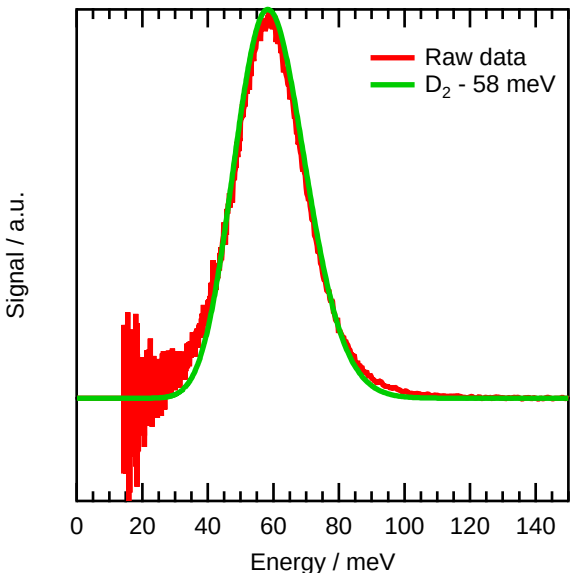

Figure 2.12: Example flux-weighted D_2 kinetic energy distribution of the transformed raw data and the resulting fit for a pure D_2 supersonic molecular beam. The most probable E_{kin} (FWHM) is 58.3 (25.2) meV .

Using this procedure, we extract kinetic energy distributions, exemplified by those shown in figure 2.12. Kinetic energy distributions of the beams used in chapters 3, 4, and 5 are included in their respective appendices.

King and Wells

Initial sticking probabilities in chapters 3, 4, and 5 are measured using the standard King and Wells (KW) method.[11] Figure 2.13 shows two exemplary KW traces for D_2 from chapter 3, as measured with the QMS. In the KW method, two beam flags are used to modulate the molecular beam. Figure 2.1 shows where the two inert flags are both located. The first flag either blocks the beam in SSB2, or lets the beam pass into the main chamber. As the molecular beam enters the main chamber, the molecular beam scatters off the second inert beam flag and increases the D_2 partial pressure. (t = -5 – 0 s) The measured stable (partial) pressure is proportional to the total flux incident entering the main chamber. After a few seconds,

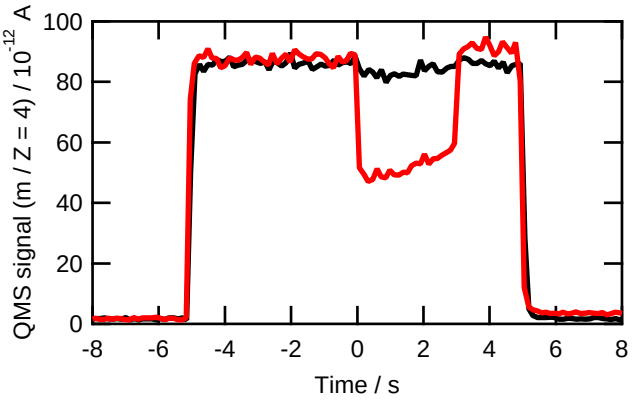

Figure 2.13: Two exemplary D_2 King and Wells experiments for high (red) and low (black) step density surfaces.

the second flag is retracted at t = 0 s so that the D_2 beam impinges onto the sample. Molecules that either remain behind at the surface due to (dissociative) adsorption or react to form a different product lower the partial pressure of D_2, and hence the D_2 flux, by a fraction. The King and Wells experiment is stopped by closing the second flag at t = 3 s and closing the first flag at t = 5 s

For chapters 3 and 4, the two beam flags are computer controlled with Labview to ensure that the time delay between opening and closing is well-defined. The resulting measured sticking curves are much more reproducible than manual controlled beam flags (chapter 5). Therefore, we can use signal averaging of multiple measurements to increase signal-to-noise levels.[46] With a curved single crystal surface, we can then measure sticking curves at up to 8 different crystal positions (surface structures) consecutively in one experiment. After each experiment with 7 or 8 surface structures probed, we flash the crystal to desorb all adsorbed molecules. For chapters 3 and 4, we perform a sputter and anneal cycle after 8 experiments.

Sticking on surfaces with low step density show the strongest time (coverage) dependence in chapter 3. Consequently, we start every sticking experiment at or nearest to the (1 1 1) apex and expose the crystal to the molecular beam for only 3 s at each position. We probe different surface structures on the crystal by moving the crystal with respect to the beam, starting from the apex, in one direction in 1 mm increments. In this way, we measure sticking probabilities for a number of relative crystal positions (and different surface structures) in one experiment, e.g. 0 mm (1 1 1), +1 mm, +2 mm, +3 mm, -3 mm, -2 mm, -1 mm. Consecutive experiments are performed in reverse order, but still start at or close to the (1 1 1) surface. We observe no difference in S_0 between experiments performed in normal or reverse order.

Results from the King and Wells experiments are normalized to the total flux and inverted, yielding time (coverage) dependent sticking traces. Two typical sticking traces for surfaces containing A- or B-type step edges are shown in figure 2.14 along with the fits used to extrapolate to $S_0(D_2)$ in chapter 3. S_0 is extracted from these time (coverage) dependent data by extrapolating a linear least squares fit to t = 0 s:

$$S(t) = S_0 + \frac{dS}{dt} \cdot t \tag{2.16}$$

There is an error in S_0 due to an uncertainty in the slope and the intercept. An additional error is introduced in t = 0, because the mass spectrometer measures ~ 7 data per second. We assume that the flag, and hence S_0, occurs at t = 0 s. We calculate the error propagation in the usual way for multiplication and summation.

We determine reaction probabilities in a similar fashion for reactions at surfaces in chapters 4 and 5. The reactant partial pressure (D_2 for chapter 4 and O_2 and HD for chapter 5) decrease as they are consumed in surface reactions. For chapter 4, we again measure the average partial pressure fraction consumed when opening the second beam flag to determine the consumption probability. The same applies for chapter 5, but two

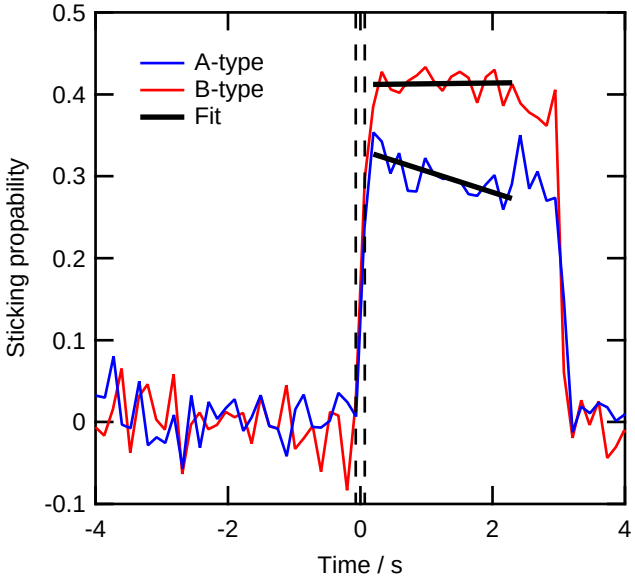

Figure 2.14: Typical signal averaged sticking traces are shown in blue and red for A- and B-type step edges. The black linear fit is extrapolated to t = 0. The dashed lines indicate the error in determining t = 0.

molecular beams are used in conjunction. There, the KW method requires normalization under identical experimental conditions, i.e. identical incident flux from both molecular beams with the second flag open and closed. Appendices C and D elaborate on the methods used to extract reaction probabilities for these experiments.